Analytical theory of the space-charge region of lateral p-n junctions in nanofilms

Vijaya Kumar Gurugubelli and Shreepad Karmalkar

Citation: J. Appl. Phys. **118**, 034503 (2015); doi: 10.1063/1.4926478
View online: http://dx.doi.org/10.1063/1.4926478
View Table of Contents: http://aip.scitation.org/toc/jap/118/3
Published by the American Institute of Physics

Analytical theory of the space-charge region of lateral *p-n* junctions in nanofilms

Vijaya Kumar Gurugubelli[a] and Shreepad Karmalkar
Department of Electrical Engineering, Indian Institute of Technology Madras, Chennai 600036, India

(Received 10 April 2015; accepted 27 June 2015; published online 15 July 2015)

There is growing interest in fabricating conventional semiconductor devices in a nanofilm which could be a 3D material with one reduced dimension (e.g., silicon-on-insulator (SOI) film), or single/multiple layers of a 2D material (e.g., MoS_2), or a two dimensional electron gas/two dimensional hole gas (2DEG/2DHG) layer. Lateral p-n junctions are essential parts of these devices. The space-charge region electrostatics in these *nanofilm* junctions is strongly affected by the surrounding field, unlike in *bulk* junctions. Current device physics of nanofilms lacks a simple analytical theory of this 2D electrostatics of lateral p-n junctions. We present such a theory taking into account the film's thickness, permittivity, doping, interface charge, and possibly different ambient permittivities on film's either side. In analogy to the textbook theory of the 1D electrostatics of bulk p-n junctions, our theory yields simple formulas for the depletion width, the extent of space-charge tails beyond this width, and the screening length associated with the space-charge layer in nanofilm junctions; these formulas agree with numerical simulations and measurements. Our theory introduces an electrostatic thickness index to classify nanofilms into sheets, bulk and intermediate sized. [http://dx.doi.org/10.1063/1.4926478]

I. INTRODUCTION

The theory of the Space-Charge Region (SCR) electrostatics in bulk *p-n* junctions (see Fig. 1(a)), based on a one-dimensional (1D) analysis, is available in text books, e.g., see Refs. 1 and 2. This theory yields the depletion width, i.e., the SCR width approximating the SCR to be fully depleted of mobile carriers, together with the charge, field, and potential distributions over this width. The actual SCR extends beyond the depletion width due to the partially depleted space-charge tails present near the depletion edges. The theory shows the width of these tails to be on the order of Debye length. While the depletion width is useful for estimating the *p-n* junction characteristics such as charge/capacitance/field versus voltage and breakdown voltage, the width of the SCR tails is useful for accurate estimation of the onset of phenomena which depend upon electrostatic interaction between adjacent junctions of the device.[3] Junctions interact electrostatically, if they are close enough for their SCR tails to overlap. Examples of phenomena based on such an interaction include the gate control of channel charge in junction field-effect transistor/high electron mobility transistor/metal-semiconductor field-effect transistor and the punch through in metal-oxide-semiconductor field-effect transistor/bipolar junction transistor.[1,2]

In this paper, we develop an analogous analytical theory of the electrostatics of *p-n* junction SCR in semiconductors whose thickness D is reduced to nanometer range as in nanofilm devices (see Fig. 1(b)); in this case, the surrounding field in the ambient strongly affects the electrostatics,[4] necessitating a 2D analysis to incorporate D and ambient permittivity. Such a theory is indispensable for understanding and designing nanofilm based diodes and transistors which are made of thin *p-n* junctions. The growing interest in fabricating conventional devices in nanofilms is motivated by the fact that nanofilm devices are suitable for flexible electronics, and possess lower parasitics due to smaller area and higher break-down voltage due to weak screening, thus achieving high frequency and high power operation. The nanofilm could be a 3D material with one reduced dimension (e.g., silicon-on-insulator (SOI) film), or a two dimensional electron gas/two dimensional hole gas (2DEG/2DHG) layer, or single/multiple layers of a 2D material like Transition

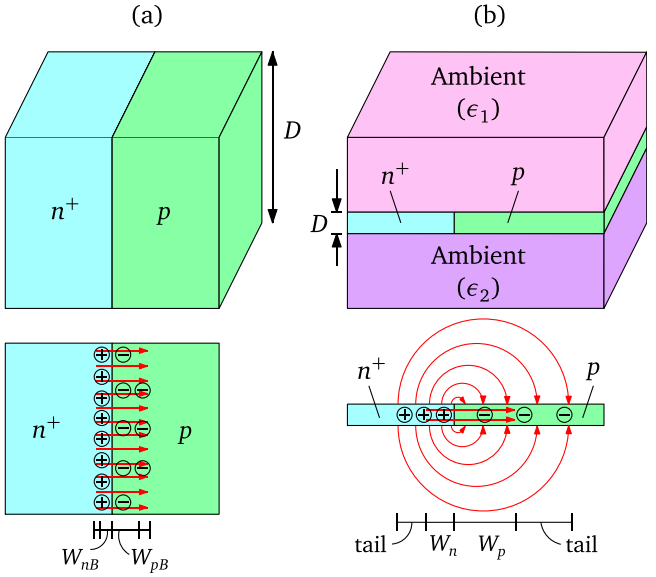

FIG. 1. Space-charge and electric field lines in (a) bulk *p-n* junction, and (b) lateral *p-n* junction in a nanofilm. The space-charge tails beyond the depletion width are also shown; these are much longer in (b) than in (a). In (b), the field lines correspond to $\epsilon_1 = \epsilon_2$. Diagrams are not to scale.

[a]Electronic mail: vkgurugubelli@gmail.com

Metal DiChalcogenide (TMDC) (e.g., MoS_2). Examples of devices in SOI nanofilms include reduced surface field diode,[5] laterally diffused metal-oxide-semiconductor,[6] and insulated-gate bipolar transistor.[7] Examples of devices in 2DEG/2DHG nanofilms include In-Plane-Gate transistors,[8] Schottky barrier heterostructure varactor diodes,[9,10] and novel photodetectors.[11] Examples of devices in 2D materials include diodes,[12,13] solar cells,[14] light emitting diode (LED),[15] and transistors.[16] These devices are either essentially *p-n* junctions or contain *p-n* junctions as essential parts. Also, their performance can be optimized by tuning the fundamental physical properties[17] like band gap and photoresponse by varying the number of 2D layers or equivalently the film thickness (amounting to D varying from less than a nanometer to tens of nanometers). Consequently, our theory analyzing a *p-n* junction including the effect of film thickness D should be of high current interest.

The 1D text-book theory[1,2] of the SCR electrostatics in an abrupt uniformly doped bulk *p-n* junction (see Fig. 1(a)) gives the following results. The *p*-side depletion width W_{pB} (B for bulk) for a given total SCR potential drop V_d is obtained using

$$V_d = \frac{qN_A W_{pB}^2}{2\epsilon_s}\left[1+\frac{N_A}{N_D}\right], \tag{1}$$

where N_A, N_D is the doping on *p*-, *n*-side, ϵ_s is the semiconductor permittivity, and q is the electronic charge. Based on the charge balance between the two sides of the junction, the *n*-side depletion width W_{nB} is given by

$$W_{nB} = (N_A/N_D)W_{pB}. \tag{2}$$

Over W_{pB} and W_{nB}, the field distribution is linear and the potential distribution is parabolic. The width of the SCR tails beyond the depletion width $W_{pB}+W_{nB}$ is a fraction of the depletion width, and is on the order of the screening length derived from the potential distribution in an SCR under linear screening. In general, for a non-degenerately doped semiconductor, this screening length is the Debye length, which for the *p*-side is given by[1]

$$L_{Dp} = \sqrt{\epsilon_s V_t/qN_A}, \tag{3}$$

where V_t is the thermal voltage.

In analogy to Eq. (1) for the *bulk* junction, our theory developed in this paper yields the following relation to estimate W_p for a given V_d in an abrupt uniformly doped lateral *p-n* junction in a *nanofilm* of thickness D

$$V_d = \frac{qN_A W_p^2}{2\epsilon_s}\left[\frac{1}{1+\left(\frac{4}{\pi}\frac{\epsilon_a}{\epsilon_s}\frac{W_p}{D}\right)}+\frac{\frac{N_A}{N_D}}{1+\left(\frac{4}{\pi}\frac{\epsilon_a}{\epsilon_s}\frac{W_p}{D}\right)\frac{N_A}{N_D}}\right], \tag{4}$$

where ϵ_a is the ambient permittivity ($\epsilon_1=\epsilon_2=\epsilon_a$ in Fig. 1(b)). W_n is obtained using Eqs. (2) and (4) based on the charge balance principle. The theory introduces an Electrostatic Thickness Index (ETI) to classify nanofilms into sheets, bulk and intermediate sized. In SCR of sheet-like films, our theory shows that the SCR tails are ten times the depletion width, i.e., much longer than in the bulk case, and the screening length analogous to L_{Dp} of the bulk case (Eq. (3)) is given by

$$L_{Fp} = 2(\epsilon_a/\epsilon_s)L_{Dp}^2/D; \tag{5}$$

it turns out that L_{Fp} is longer than L_{Dp}, and the SCR tail width can be hundreds of L_{Fp}.

In practice, ambient permittivities above and below the film could be different, there could be a charge along the nanofilm-ambient interface, and the junctions realized in sheets would be affected by quantum confinement and degenerate doping. We show how our theory can be adapted to incorporate these practical variations. The theory can also be used for a Schottky junction in a nanofilm; examples of lateral metal-nanofilm junctions include an end/edge contact to Graphene[18] or MoS_2 device.[19] We validate our theory by comparing it with accurate self-consistent numerical simulations, measurements, and prior theoretical works.

II. STRUCTURAL PARAMETERS, EQUATIONS, AND APPROXIMATIONS

We consider an abrupt uniformly doped *p-n* junction in this paper; linearly graded junction will be considered in a separate work. Refer to the nanofilm *p-n* junction shown in Fig. 1(b). The electrostatics of a nanofilm junction depends on the parameters of the bulk junction, namely—potential drop $V_d = V_{bi} - V_a$, where $V_{bi} = V_t \ln(N_A N_D/n_i^2)$ is the built-in potential and V_a is the applied voltage, N_A, N_D, and ϵ_s, and in addition, D, ambient permittivities ϵ_1 above and ϵ_2 below the film, and film-ambient interface charge σ_f. For simplicity, we first consider the case of $\epsilon_1=\epsilon_2=\epsilon_a$ and $\sigma_f=0$. Later, we show that these results apply to the case of $\epsilon_1 \neq \epsilon_2$ if we replace ϵ_1 and ϵ_2 by $\epsilon_{eff}=(\epsilon_1+\epsilon_2)/2$. Finally, we consider the effect of nonzero σ_f.

The potential distribution φ is governed by Poisson's equation in the film ($\nabla^2\varphi = -\rho/\epsilon_s$, where ρ is the space-charge density) and Laplace's equation in the ambient ($\nabla^2\varphi = 0$). A semi-classical treatment suffices since our theory derives the relationship between φ and V_d, N_A, N_D and D. The factors such as quantum confinement and density

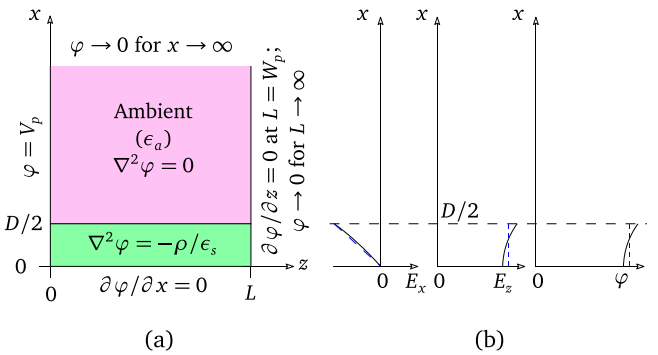

FIG. 2. (a) The governing equations and boundary conditions for the upper half cross-section of the *p*-side of the nanofilm junction shown in Fig. 1(b); $\epsilon_1=\epsilon_2=\epsilon_a$ is assumed. (b) Variations of actual (solid lines) and approximated (dashed lines) E_x, E_z, and φ over film thickness ($x \le D/2$); see text for the details of approximations.

of states change the value of V_d but leave this relationship intact. Hence, we develop our theory for a non-degenerately doped film, and point out modifications required to treat quantum confinement and degenerate doping effects. Refer to Fig. 2(a), which shows the coordinate system for $\epsilon_1 = \epsilon_2 = \epsilon_a$. The x-axis is vertical along the junction, and the z-axis is horizontal along the middle of the film. Inside the film, we find it convenient to work with the electric field, and hence, we write the Poisson's equation in the form of Gauss's law. Assuming that the quantities do not vary along y, the Gauss's law inside the film is

$$\frac{\partial E_x}{\partial x} + \frac{\partial E_z}{\partial z} = \frac{\rho}{\epsilon_s}. \tag{6}$$

Our numerical simulations show that, so long as $D \lesssim W_{pB}$, for $x \le D/2$, we can approximate E_x to vary linearly with x from $E_x = 0$ at $x = 0$, and φ and E_z to be constant with x (see Fig. 2(b)). $E_x = 0$ at $x = 0$ due to structural symmetry. Note that a linear E_x vs x implies a parabolic φ vs x. However, the variation in φ over the film thickness is much smaller than the magnitude of φ, which is why φ can be approximated to be constant over the film thickness. Our linear approximation of E_x is not the derivative of this constant approximate φ, but rather, an approximation of the derivative of the actual φ. Including σ_f, the linear E_x versus x assumption implies

$$\frac{\partial E_x(x,z)}{\partial x} \approx \frac{E_x(D/2^-,z)}{D/2} = -\frac{2}{D}\frac{\epsilon_a}{\epsilon_s}\frac{\partial \varphi(D/2^+,z)}{\partial x} - \frac{2\sigma_f}{D\epsilon_s}. \tag{7}$$

The constant E_z versus x assumption implies

$$\frac{\partial E_z(x,z)}{\partial z} \approx \frac{\partial E_z(D/2^-,z)}{\partial z} = -\frac{\partial^2 \varphi(D/2^+,z)}{\partial z^2}. \tag{8}$$

Substitution of Eqs. (7) and (8) into Eq. (6) leads to

$$\frac{2}{D}\frac{\epsilon_a}{\epsilon_s}\frac{\partial \varphi(D/2^+,z)}{\partial x} + \frac{\partial^2 \varphi(D/2^+,z)}{\partial z^2} = -\frac{(\rho + 2\sigma_f/D)}{\epsilon_s}, \tag{9}$$

which needs to be solved to obtain $\varphi(D/2^+, z)$.

III. JUNCTION DEPLETION WIDTH

A. Model

Let V_p and V_n denote the components of V_d on the p and n sides, i.e.,

$$V_d = V_p + V_n. \tag{10}$$

Without any loss of generality, we regard the p-side to be lightly doped relative to the n-side and analyze the p-side to derive a relation between V_p and W_p. A similar analysis on the n-side would yield an analogous relation between V_n and W_n. These relations together with Eqs. (2) and (10) lead to Eq. (4).

Refer to Fig. 2(a). The symmetry associated with the condition $\epsilon_1 = \epsilon_2$ allows us to consider only the upper half of the film. Consider the boundary conditions associated with the upper half of the p-side. We have $E_x = 0$ at $x = 0$, and $\varphi \to 0$ for $x \to \infty$. We approximate that, even when $N_A \neq N_D$, the plane $z = 0$ along the junction remains equipotential as in the symmetric case $N_A = N_D$. Let $\varphi = V_p$ be the potential along the plane $z = 0$. This implies that the boundary condition for $z \to \infty$ is $\varphi \to 0$, which however does not yield an analytical solution. Hence, we employ a different boundary condition $\partial\varphi/\partial z = 0$ at $z = W_p$, i.e., no field line crosses the plane $z = W_p$. This condition is a result of the complete depletion approximation, i.e.,

$$\rho(x,z) = \begin{cases} -qN_A & \text{for} \quad 0 < z \le W_p, \\ 0 & \text{for} \quad z > W_p. \end{cases} \tag{11}$$

Note that, $\varphi = 0$ at $(x, z) = (0, W_p)$, but we cannot assume $\varphi = 0$ over the entire plane $z = W_p$ because of the existence of a field component along this plane.

For the above boundary conditions, the general solution of Laplace's equation in the ambient is

$$\varphi(x \ge D/2, z) = V_p - \sum_{m=0}^{\infty} B_m \sin(k_m z) e^{-k_m(x-D/2)}, \tag{12}$$

where $k_m = (2m+1)\pi/2W_p$. Substitution of $\rho = -qN_A$ from Eq. (11), $\sigma_f = 0$ and Eq. (12) in Eq. (9) results in an equation for B_m, which can be solved using Fourier series techniques to obtain

$$B_m = \frac{16}{\pi^3}\frac{qN_A W_p^2}{\epsilon_s}\frac{1}{(2m+1)^3\left[1 + \frac{2}{\pi}\frac{\epsilon_a}{\epsilon_s}\frac{W_p}{D}\frac{2}{2m+1}\right]}. \tag{13}$$

From the previous paragraph, $\varphi(0, W_p) = 0$, which implies $\varphi(D/2, W_p) \approx 0$ because of the approximation that φ is almost constant over the film thickness. Setting $\varphi(D/2, W_p) \approx 0$ in Eq. (12), we get $V_p = \sum_0^\infty (-1)^m B_m$, where B_m is given by Eq. (13). In this summation, the term with $m = 0$, i.e., B_0, dominates. Hence, we write V_p in terms of B_0 as $V_p \approx \alpha B_0$, where α is a factor close to one. Since we should have $V_p = qN_A W_p^2/2\epsilon_s$ for $D \to \infty$, i.e., the limiting case of bulk, we obtain $\alpha = \sum_0^\infty (-1)^m/(2m+1)^3 = \pi^3/32 \approx 0.97$. Using Eq. (13) and $V_p = \alpha B_0$, we obtain the relation between V_p and W_p as

$$V_p = \frac{qN_A W_p^2}{2\epsilon_s}\frac{1}{1 + \frac{4}{\pi}\frac{\epsilon_a}{\epsilon_s}\frac{W_p}{D}}. \tag{14}$$

A similar analysis on the n-side would yield the relation between V_n and W_n as Eq. (14) with V_p and W_p replaced by V_n and W_n. From Eqs. (2), (10), and (14), we obtain Eq. (4) relating V_d and W_p. Note that, for the limiting case of large D or $\epsilon_a \ll \epsilon_s$, Eq. (4) of the film reduces to Eq. (1) of the bulk as it should, and so, W_p approaches its value W_{pB} in a bulk junction. For small D, we can neglect the unity term in the denominator of the two RHS terms of Eq. (4) to obtain

$$W_p \approx \frac{4}{\pi}\frac{\epsilon_a V_d}{qN_A D} = \frac{4}{\pi}\frac{\epsilon_a V_d}{qN_S}, \tag{15}$$

where the latter form of equation is useful when films are characterized by surface doping $N_S = N_A D$ rather than

volume doping N_A and thickness D. This W_p is independent of ϵ_s, and hence can be regarded as corresponding to sheet-like films. Moreover, this equation predicts $W_p \propto 1/D$, and $W_p \propto V_d/N_A$ in contrast to $W_{pB} \propto \sqrt{V_d/[N_A(1+N_A/N_D)]}$ as per Eq. (1) for the bulk case.

From Eq. (4) and the above discussion, it is seen that whether the electrostatics of a film is bulk-like or sheet-like depends not on the absolute value of D but on the value of D relative to W_p and on ϵ_s/ϵ_a. Hence, we classify films as bulk, sheet or intermediate sized based on the single parameter

$$\eta = \epsilon_s D/\epsilon_a W_{pB}\,, \tag{16}$$

which we call Electrostatic Thickness Index (ETI). Identification of a film as bulk-like or sheet-like allows the use of simple Eqs. (1) or (15), respectively. The values of η for this classification will be derived following the derivation of W_p for a general case.

To derive W_p of a general nanofilm junction, we write Eq. (4) in a normalized form in terms of W_p/W_{pB}, η and doping asymmetry factor $a = N_A/N_D$ as

$$(1+a) = \left(\frac{W_p}{W_{pB}}\right)^2 \left[\frac{1}{1+\frac{4}{\pi\eta}\frac{W_p}{W_{pB}}} + \frac{a}{1+\frac{4a}{\pi\eta}\frac{W_p}{W_{pB}}}\right]. \tag{17}$$

Recall that the p-side is lightly doped in our analysis. If the n-side were lightly doped, the above equation would have been for W_n in terms of W_{nB}, $\eta = \epsilon_s D/\epsilon_a W_{nB}$ and $a = N_D/N_A$, so that $a \le 1$ always. We rearrange Eq. (17) in the form of the cubic equation

$$\frac{8a}{\pi\eta}\left(\frac{W_p}{W_{pB}}\right)^3 + (1+a)\left(1-\frac{16a}{\pi^2\eta^2}\right)\left(\frac{W_p}{W_{pB}}\right)^2 - \frac{4(1+a)^2}{\pi\eta}\left(\frac{W_p}{W_{pB}}\right) - (1+a) = 0\,. \tag{18}$$

In general, W_p/W_{pB} is the positive real root of this equation. As per the theory of cubic equations,[20] this equation has a single positive real root for the following three reasons: the discriminant of this cubic equation > 0 implying that all its roots are real; the derivative of the LHS function has one positive and one negative zero implying that the cubic equation has at least one negative real root; the product of the three roots of this cubic equation, given by the negative of the ratio of the constant term to the coefficient of the cubic term, is positive implying that there are two negative and one positive real roots. This positive real root for W_p/W_{pB} turns out to be lengthy when expressed in closed-form. Hence, it is better to directly solve Eq. (18) using a scientific hand calculator. For the special case of symmetric junction ($a = 1$), the closed-form solution simplifies to

$$\frac{W_p}{W_{pB}} = \frac{2}{\pi\eta} + \sqrt{\left(\frac{2}{\pi\eta}\right)^2 + 1}\,, \tag{19}$$

which can also be obtained from the quadratic equation resulting from substituting $V_p = V_d/2$ in Eq. (14). Fig. 3(a) plots W_p/W_{pB} versus η obtained from Eq. (18) for various values of a.

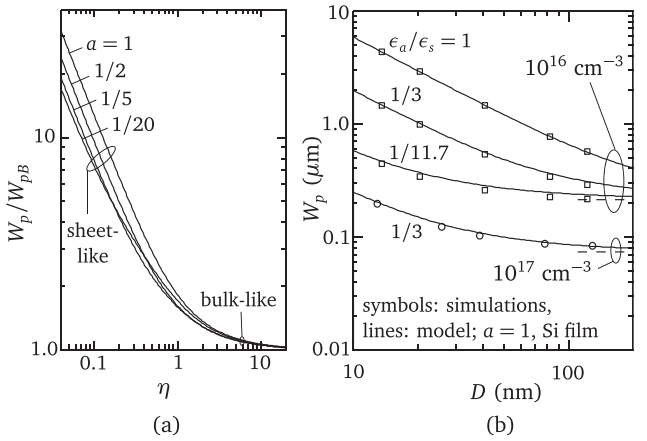

FIG. 3. (a) The normalized depletion width W_p/W_{pB} versus ETI behavior obtained from Eq. (18) for various doping asymmetry factors; sheet-like and bulk-like limits of the behavior are indicated; the sheet-like behavior is a straight line on a log-log plot. (b) Equilibrium depletion width W_p versus thickness D behavior obtained from Eq. (19) for a symmetric p-n junction; results are shown for different doping levels and ambient permittivities; solid lines are the model Eq. (19), symbols are simulations and dashed lines indicate bulk-limits.

B. Classification of films

We now discuss the derivation of the following formulas used to classify films into bulk-like, sheet-like and intermediate sized in Fig. 3(a)

$$\begin{aligned} &\eta \ge \frac{360(1+a^2)}{19\pi(1+a)} \quad \text{bulk–like,} \\ &\eta \le \frac{4}{3\pi}\sqrt{\frac{a(1+a)(5-4a)}{1+a^2}} \quad \text{sheet–like,} \\ &\text{otherwise} \quad \text{intermediate sized.} \end{aligned} \tag{20}$$

Once a film is identified as bulk-like or sheet-like, the simple formulas Eq. (1) or Eq. (15) can be used, respectively, instead of the general cubic equation Eq. (18), which however has to be used if the film is intermediate sized. The minimum η for bulk-like films is solved for from Eq. (17) as the value for which W_p approaches W_{pB} within 10%, i.e., $W_p/W_{pB} = 10/9$; to simplify the solution, we use the approximation $1/(1+u) \approx (1-u)$ for small u, for the two terms in the brackets of Eq. (17). The maximum η for sheet-like films is solved for from Eq. (17) as the value for which W_p approaches within 10% of its value for sheet-like films given by Eq. (15), i.e., $W_p/W_{pB} = (10/9)[2(1+a)/\pi\eta]$ from Eqs. (15) and (1); to simplify the solution, we use the approximation $1/(1+u) \approx u^{-1}(1-u^{-1})$ for large u. As per Eq. (20), for $1/20 \le a \le 1$, the bulk-limit for η lies in the range 5 to 6, and the sheet-limit lies in the range 0.2 to 0.6.

An example illustrates the significance of this classification: a silicon film with $D = 130\,\text{nm}$, $N_A = 10^{16}\,\text{cm}^{-3}$ and $a = 1$ is bulk-like for $\epsilon_a = 1$ since $\eta = 7.1$, and sheet-like for $\epsilon_a = 18$ (HfO_2) since $\eta = 0.4$; $W_p = 0.23$, $0.75\,\mu\text{m}$ in the bulk-, sheet-like cases.

TABLE I. Comparison between the equilibrium depletion widths W_p obtained from our model (Eq. (18)) and simulations for asymmetric p-n junctions in a silicon nanofilm with SiO_2 ambient. W_{pB} given here is calculated from Eq. (1).

N_A (cm^{-3})	$a = N_A/N_D$	W_{pB} (μm)	D/W_{pB}	W_p/W_{pB}		
				Mod	Sim	% err
10^{16}	1	0.214	0.064	6.804	6.818	−0.20
…	…	…	0.191	2.612	2.514	3.90
…	…	…	0.572	1.439	1.350	6.59
…	1/5	0.284	0.048	5.648	6.598	−14.4
…	…	…	0.144	2.426	2.472	−1.86
…	…	…	0.431	1.461	1.348	8.38
…	1/10	0.301	0.045	5.654	6.505	−13.1
…	…	…	0.136	2.575	2.445	5.32
…	…	…	0.408	1.525	1.339	13.9
…	1/20	0.312	0.044	5.901	6.478	−8.91
…	…	…	0.131	2.798	2.442	14.6
…	…	…	0.394	1.590	1.340	18.7
10^{17}	1	0.073	0.176	2.767	2.699	2.52
…	…	…	0.353	1.767	1.685	4.87
…	…	…	0.530	1.479	1.397	5.87
…	1/5	0.097	0.133	2.536	2.618	−3.13
…	…	…	0.267	1.742	1.649	5.64
…	…	…	0.400	1.484	1.381	7.46

C. Model validation

Fig. 3(b) compares W_p as a function of D calculated from Eq. (19) with TCAD simulations for symmetric junctions with typical doping levels and permittivities. Similarly, Table I compares W_p calculated from Eq. (18) with TCAD simulations for typical asymmetric junctions. We see that D and ϵ_a can change W_p by an order of magnitude each. The simulated values of W_p reported here are obtained by self-consistent solution[21] of the Poisson's equation and drift-diffusion transport equations,[2] and need an explanation. In a bulk p-n junction, W_{pB} estimated using Eq. (1) is $\approx \int |\rho| dz/qN_A$ obtained from simulations. However, in a nanofilm junction, where the SCR tail is rather long due to weak screening, the W_p extracted from simulations using $W_p = \int |\rho| dz/qN_A$ turns out to be unphysically large. Therefore, we need an alternate criterion. We note that, in the p-side of a bulk junction, the simulated space-charge falls to $\sim 45\%$ of $-qN_A$ at the edge of the depletion width W_{pB} calculated analytically from Eq. (1). Applying an analogous % criterion, we find that the simulated space-charge in the p-side of a thin nanofilm junction falls to $\sim 55\%$ of $-qN_A$ at the edge of the depletion width W_p calculated analytically from Eq. (18) or (19). As film thickness D increases, middle of the film ($x = 0$) gets progressively screened from the surface ($x = D/2$), causing the simulated depletion width along the middle to be less than that along the surface. The simulated W_p reported in Fig. 3(b) and Table I is the average of these two different widths. We see that the match between analytically calculated and simulated values is good. This agreement confirms the validity of our basic approximations that, over the film thickness, the potential and axial field are uniform and the normal field varies linearly. The error increases with doping asymmetry because the constant potential boundary condition $\varphi = V_p$ on the plane $z = 0$ is perfect for a symmetric junction but becomes progressively approximate with increase in doping asymmetry. In Table I, the values of W_p for $N_D/N_A = 10, 20$ ($a = 1/10, 1/20$) indicate that the depletion width on the lightly doped side of the junction tends to saturate with increase in asymmetry beyond $N_D/N_A = 10$ because the lightly doped side gets inverted near the junction.[22] Thus, for $N_D/N_A > 20$ ($a < 1/20$), W_p can be approximated as the value obtained for $a = 1/20$ from Eq. (18).

IV. SPACE-CHARGE TAIL

A. Model

As pointed out in the introduction, the actual SCR extends beyond the depletion width $W_p + W_n$ derived above, due to the partially depleted space-charge tails present near the depletion edges. The width of these tails has to be taken into account for accurate estimation of the onset of phenomena which depend upon electrostatic interaction between adjacent junctions of the device.[3] Without any loss of generality, we derive the width of the SCR tail in the p-side of the nanofilm p-n junction; similar derivation applies to the n-side.

Refer to Fig. 4(a). Let W_{pt} (t for tail) denote the distance from the junction at which the space-charge density falls to a

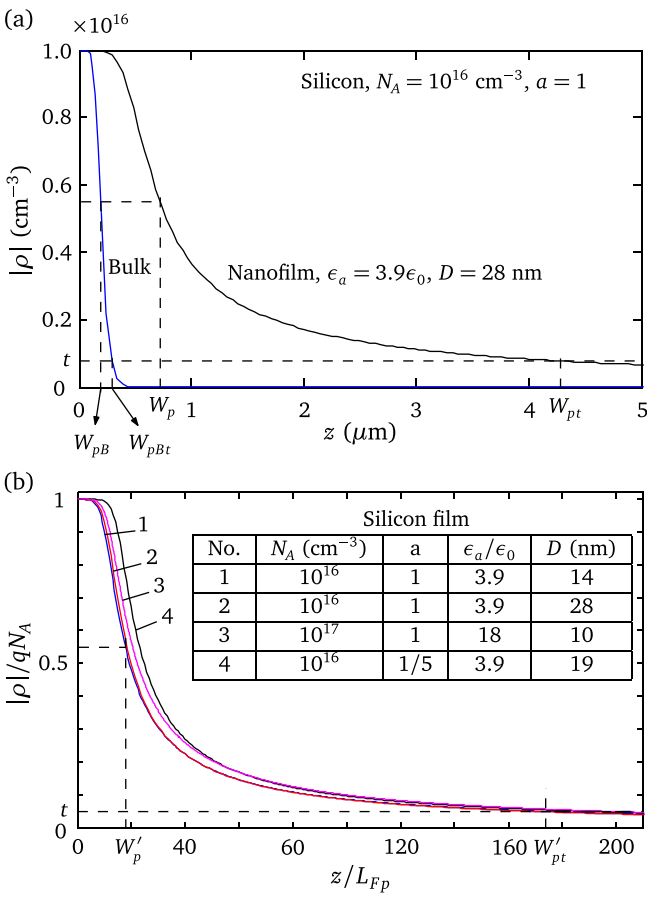

FIG. 4. The simulated p-side space-charge distribution under equilibrium as a function of distance from the junction; the depletion widths and space-charge tails are indicated. (a) Distributions in bulk and nanofilm junctions. (b) Normalized form of the distributions in sheet-like films illustrating the utility of screening length L_{Fp}; W_p' and W_{pt}' are indicated for curve 1.

fraction $t \leq 0.1$ of its peak value, i.e., $\rho(D/2, W_{pt}) = -tqN_A$. We define the width of the SCR tail as $W_{pt} - W_p$, where W_p is the depletion width derived earlier in this paper. For ρ as small as $|\rho| \leq tqN_A$, linear screening prevails, i.e., ρ is proportional to φ as per $\rho = q^2(\partial p/\partial E_F)\varphi$, where p is the hole density and E_F is the Fermi-level.[23] When doping is non-degenerate, p is given by the Boltzmann distribution, and so, $\partial p/\partial E_F = -p/qV_t = -N_A/qV_t$. Substituting this in $\rho = q^2(\partial p/\partial E_F)\varphi$ and using Eq. (3), we have

$$\rho = q^2(\partial p/\partial E_F)\varphi = -\epsilon_s\varphi/L_{Dp}^2 . \tag{21}$$

Using $\rho(D/2, W_{pt}) = -tqN_A$ in this equation, we have

$$\varphi(D/2, W_{pt}) = -L_{Dp}^2\rho(D/2, W_{pt})/\epsilon_s = tV_t , \tag{22}$$

which yields W_{pt} from the knowledge of φ.

The boundary conditions to solve for φ, shown in Fig. 2(a), are $E_x = 0$ at $x = 0$, $\varphi \to 0$ for $x \to \infty$, $\varphi = V_p$ at $z = 0$ and $\varphi \to 0$ for $z \to \infty$. The latter boundary condition differs from the condition $\partial\varphi/\partial z = 0$ at $z = W_p$ employed in W_p derivation, since we need φ over the space-charge tail beyond W_p. For these boundary conditions, the general solution of Laplace's equation in the ambient is

$$\varphi(x \geq D/2, z) = V_p - \int_0^\infty A(\lambda)\sin(\lambda z)e^{-\lambda(x-D/2)}d\lambda . \tag{23}$$

It is difficult to obtain φ for all values of z since $A(\lambda)$ is not known for all values of λ, because variation of ρ between $z = W_p$ and $z = W_{pt}$ is not known. However, we can obtian φ in the region $z \geq W_{pt}$ of our interest from an approximate expression of $A(\lambda)$ for small λ. This is because only small values of λ contribute to the integral in Eq. (23) for $z \geq W_{pt}$, since z is large and $\sin(\lambda z)$ is an osciallatory function. Substitution of Eq. (23) for φ along with $\rho = -\epsilon_s\varphi/L_{Dp}^2$ (from Eq. (21)) and $\sigma_f = 0$ in Eq. (9) results in the following equation valid for $z \geq W_{pt}$:

$$\int_0^\infty V_p^{-1}[1 + L_{Fp}\lambda + L_{Dp}^2\lambda^2]A(\lambda)\sin(\lambda z)d\lambda = 1 , \tag{24}$$

where L_{Fp} was introduced in Eq. (5) as the screening length in sheet-like films analogous to the Debye length L_{Dp} in the bulk; the significance of L_{Fp} is discussed in Sec. V. Comparing Eq. (24) with the mathematical identity $\int_0^\infty [2\sin(\lambda z)/\pi\lambda]d\lambda = 1$ for $z > 0$, we obtain $A(\lambda)$ for small λ as

$$A(\lambda) = \frac{2V_p}{\pi\lambda}\left[1 + L_{Fp}\lambda + L_{Dp}^2\lambda^2\right]^{-1} . \tag{25}$$

From Eqs. (23) and (25), we get φ for $z \geq W_{pt}$ as

$$\frac{\varphi(D/2^+, z)}{V_p} = 1 - \frac{2}{\pi}\int_0^\infty \frac{\sin(\lambda z)}{\lambda\left(1 + L_{Fp}\lambda + L_{Dp}^2\lambda^2\right)}d\lambda . \tag{26}$$

We can obtain W_{pt} from this equation numerically by substituting $z = W_{pt}$, taking an appropriate value of t, e.g., $t = 0.05$ (5% of $-qN_A$), and noting that the LHS $= tV_t/V_p$ from Eq. (22), where V_p is given by Eq. (14) and W_p is calculated as discussed in Sec. III A.

For the limiting case of sheet-like films, i.e., small D, an explicit expression for W_{pt} can be derived as follows. Considering that only small λ contribute to the integral in Eq. (26), for small D, we can approximate $1 + L_{Fp}\lambda + L_{Dp}^2\lambda^2 \approx 1 + L_{Fp}\lambda$ in Eq. (26) to obtain

$$\frac{tV_t}{V_p} \approx \frac{2}{\pi}\mathrm{Ci}\left(W'_{pt}\right)\sin\left(W'_{pt}\right) + \cos\left(W'_{pt}\right)\left[1 - \frac{2}{\pi}\mathrm{Si}\left(W'_{pt}\right)\right], \tag{27}$$

where Ci and Si are Cosine and Sine Integrals, and $W'_{pt} = W_{pt}/L_{Fp}$. Using the asymptotic series expansions of Ci and Si for large arguments and neglecting the higher order terms, we get

$$\frac{tV_t}{V_p} \approx \frac{2}{\pi}\frac{1}{W'_{pt}} = \frac{2}{\pi}\frac{L_{Fp}}{W_{pt}} . \tag{28}$$

In this equation, we substitute for L_{Fp} from Eq. (5) and $V_p \approx \pi qN_ADW_p/8\epsilon_a$ obtained from Eq. (14) for sheet-like films to derive W_{pt} as

$$W_{pt} = \frac{W_p}{2t} = \frac{2\epsilon_aV_d}{\pi tqN_AD} = \frac{2\epsilon_aV_d}{\pi tqN_S} . \tag{29}$$

By way of example, we estimate the junction SCR tail widths in sheet- and bulk-like films for $V_p = 0.35$ V, taking $t = 0.05$, and $V_t = 26$ mV. In sheet-like films, the tail width $= W_{pt} - W_p = W_p(0.5t^{-1} - 1) = 9W_p$, where W_p is many times W_{pB}. In contrast, the tail width in bulk junction is[3] $1.13L_{Dp}\ln[(0.525/t)\sqrt{V_t/2V_p}] = 0.8L_{Dp}$, which is just 1/6.5 times $W_{pB} = L_{Dp}\sqrt{2V_p/V_t} = 5.2L_{Dp}$.

B. Model Validation

For the junctions (1)–(4) tabulated in the inset of Fig. 4(b), we estimate W_{pt} using Eq. (29) with $V_d = V_{bi}$ and $t = 0.05$ as: (1) 13.6 μm, (2) 6.8 μm, (3) 10.5 μm, and (4) 10.9 μm. The corresponding simulated values turn out to be (1) 13.6 μm, (2) 6.7 μm, (3) 10.3 μm, and (4) 11.1 μm. It is seen that our theory predicts the simulated values within 2%.

V. SCREENING LENGTH

Using the series of approximations employed to derive Eq. (28) from Eq. (26), we can simplify Eq. (26) to obtain a hyperbolic dependence of φ on z for large z as

$$\frac{\varphi\left(D/2^+, \text{large } z\right)}{V_p} \approx \frac{2}{\pi}\frac{1}{\left(z/L_{Fp}\right)} . \tag{30}$$

Considering that $\rho \propto \varphi$ under linear screening, the inverse proportionality of φ to D in Eq. (30) suggests a strong dependence of charge density, and hence junction capacitance, on D.

Based on Eq. (30), we can regard L_{Fp} used in the equations of Sec. IV A as the screening length for large z. A significance of L_{Fp} is that it is a convenient normalizing

parameter for the distance away from the junction on the p-side. As shown in Fig. 4(b), the widely different space-charge distributions on the p-side of various sheet-like nano-film junctions appear close to each other, i.e., in a compact form, if plotted in the normalized form $|\rho|/qN_A$ versus z/L_{Fp} on a single graph. Further, we can express W_p and W_{pt} in terms of L_{Fp} in the same way as these quantities for a bulk junction were expressed above in terms of L_{Dp}, which is the screening length in a uniformly doped p-type bulk semiconductor. Substituting for L_{Dp} from Eq. (3) in Eq. (5), we get

$$L_{Fp} = \frac{2\epsilon_a V_t}{qN_A D} = \frac{2\epsilon_a V_t}{qN_S}, \tag{31}$$

where N_S is the surface doping characterizing a film. Using this equation, we express W_p given by Eq. (15) and W_{pt} given by Eq. (29), for sheet-like films, as

$$W_p = \left(\frac{2V_d}{\pi V_t}\right) L_{Fp} \quad \text{and} \quad W_{pt} = \left(\frac{V_d}{\pi t V_t}\right) L_{Fp}. \tag{32}$$

By way of example, taking $V_d = 0.7\,\text{V}$, $t = 0.05$, and $V_t = 26\,\text{mV}$, we get $W_p = 17.1 L_{Fp}$ and $W_{pt} = 171 L_{Fp}$ (see Fig. 4(b)).

The reason why Eq. (32) for W_p and W_{pt} and Fig. 4(b) showing the normalized space-charge distribution are restricted to sheet-like films is as follows. Eq. (30) is derived from the approximation $1 + L_{Fp}\lambda + L_{Dp}^2\lambda^2 \approx 1 + L_{Fp}\lambda$ for small λ. As D increases, this approximation is valid for progressively smaller λ, implying that Eq. (30) is valid for progressively larger z. Since W_p and W_{pt} decrease with increase in D, the space-charge at such large z is negligible. Hence, L_{Fp}, derived above as the screening length for large z, cannot be used to describe the shorter depletion widths and SCR tails occurring relatively closer to the junction in thicker films.

VI. ADDITIONAL EFFECTS

A. Quantum confinement in sheets

Our models for φ, W_p, and W_{pt} in terms of V_d, N_A, N_D, and D are obtained from a solution of Poisson's equation under certain boundary conditions. Even in the presence of quantum confinement effects, the equation and the boundary conditions remain unchanged, and so, the formulas for φ, W_p, and W_{pt} remain valid. However, these effects call for a quantitative correction in V_d for the following reason. Very small D confines the carriers in the film causing quantization of the energy levels in the conduction and valence bands. This causes the fermi-levels in p and n regions to move towards or even into the bands increasing the built-in potential, V_{bi}, which in turn increases V_d as per $V_d = V_{bi} - V_a$. Thus, the correction in V_d is the increase in V_{bi}. The increased V_{bi} due to above confinement effects is derived as follows.

For thinner films, the constant φ approximation over the film thickness is increasingly valid, so that the potential well approaches a square shape. Moreover, though the depth of the well is finite, the first subband, which is of our interest, is so deep inside the well that this subband can be obtained assuming the well depth to be infinite. For an infinitely deep square well, the solution of the Schrodinger equation yields constant subband density of states ρ_{DOS}, and the first subband minimum E_{1n} for electrons and the first subband maximum E_{1p} for holes as[24]

$$\rho_{DOS}(E) = \frac{m^*}{\pi\hbar^2} \quad \text{and} \quad \left.\begin{matrix} E_{1n} - E_C \\ E_V - E_{1p} \end{matrix}\right\} = \frac{\pi^2\hbar^2}{2m^* D^2}, \tag{33}$$

where E_C and E_V are conduction and valence band edges, and m^* is electron or hole effective mass. For simplifying the discussion ahead, an average m^* for all three directions is used in the above equations. However, the conclusions drawn hold good even when m^* appearing in ρ_{DOS} and E_{1n} or E_{1p} are different. Assuming only the first subband to be filled, the hole concentration per unit surface area on p-side is[24]

$$p_s = \frac{m_p^* q V_t}{\pi\hbar^2} \ln\left[1 + \exp\left(\frac{E_{1p} - E_F}{qV_t}\right)\right], \tag{34}$$

where m_p^* is the hole effective mass. From this equation, we can solve for E_F on p-side in terms of p_s. We can obtain E_F on n-side in terms of n_s in a similar manner. Thus, the built-in potential obtained from the Fermi-level difference between p and n sides is

$$V_{bi} = \frac{E_g}{q} + \frac{\pi^2\hbar^2}{2qD^2}\left(\frac{1}{m_n^*} + \frac{1}{m_p^*}\right) + V_t \ln\left\{\left[\exp\left(\frac{\pi\hbar^2 n_s}{m_n^* q V_t}\right) - 1\right]\left[\exp\left(\frac{\pi\hbar^2 p_s}{m_p^* q V_t}\right) - 1\right]\right\}. \tag{35}$$

We have verified with numerical calculations that the above equation for V_{bi} based on single subband occupation is accurate to within 4% of the value based on two subbands

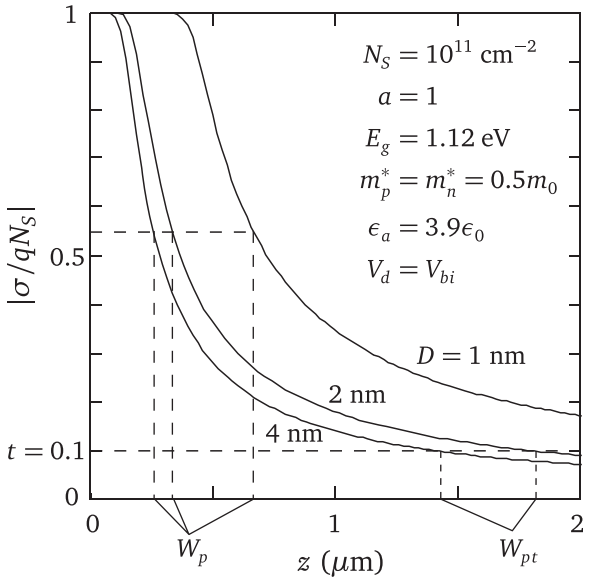

FIG. 5. The simulated p-side space-charge distribution under equilibrium as a function of distance from the junction for films of different thicknesses having quantum confinement effects; the depletion and space-charge tail widths are indicated.

occupation for carrier concentration up to 10^{13} cm^{-2} and film thickness up to 10 nm.

We can obtain W_p and W_{pt} under quantum confinement effects using Eqs. (15) and (29), respectively, taking into account the increased V_{bi} in Eq. (35). For a film with $D = 1$ nm, $n_s = p_s = N_S = 10^{11}$ cm^{-2}, and other parameter values shown in Fig. 5, the value of V_{bi} calculated using Eq. (35) is 2.4 V, which is 2.5 times the value of 0.95 V obtained from the classical formula $V_{bi} = V_t \log(N_A N_D/n_i^2)$, where $N_A = p_s/D$ and $N_D = n_s/D$ have been used. However, when the film thickness is raised to $D = 4$ nm, the V_{bi} based on Eq. (35) is just 13% higher than the classical value. Hence, for films thicker than ~5 nm, V_{bi} can be determined using the classical formula. The N_S to be used in Eqs. (15) and (29) is the ionized impurity concentration. As we move away from the junction, the extent of impurity ionization, represented by the difference between the Fermi and impurity levels, decreases and finally saturates. Therefore, N_S to be used in W_p can be different from that in W_{pt}, where saturated N_S value can be used. In certain cases, the source of N_S may not be impurities in the film but interface charges, e.g., N_S could be the 2DEG concentration resulting from the polarization charge at AlGaN/GaN interface.

To validate our theory at the quantum mechanical level, we compare the results of Eq. (15) for W_p and Eq. (29) for W_{pt} with finite-difference calculations for a symmetric p-n junction. For this purpose, we assume the film to have zero thickness, and represent the charge density in the SCR on p-side as

$$\sigma(z > 0) = q(p_s - N_S)\,, \tag{36}$$

where p_s is given by Eq. (34). Using finite-difference method, we self-consistently solve the Laplace's equation $\nabla^2\varphi = 0$ in the ambient with the boundary conditions: (i) $\partial\varphi(0^+, z)/\partial x = -\sigma/2\epsilon_a$ for $x = 0$, where σ is given by Eq. (36); (ii) $\varphi = V_p$ for $z = 0$; (iii) $\partial\varphi/\partial z = 0$ for $z = L$, where L is chosen to be greater than W_{pt} so that the charge tail goes to zero; and (iv) $\partial\varphi/\partial x = 0$ for $x = S$, where S is chosen to be $\geq L$.

Fig. 5 shows the p-side space-charge distributions obtained from these self-consistent calculations for films with different thicknesses having quantum confinement effects. For the parameters shown in Fig. 5 and $D = 4$ nm, 2 nm, and 1 nm, Eq. (15) yields $W_p = 277$ nm, 354 nm, and 664 nm, respectively, and Eq. (29) with $t = 0.1$ yields $W_{pt} = 1.38$ μm, 1.77 μm, and 3.32 μm, respectively. The corresponding simulated values turn out to be $W_p = 261$ nm, 338 nm, 668 nm and $W_{pt} = 1.39$ μm, 1.78 μm, 3.34 μm. It is seen that our theory predicts the simulated values within 6%.

We now show that L_{Fp} in Eq. (5) approaches the two-dimensional screening length in a sheet, given by[25] $L_{2D} = -2\epsilon_a/q^2(\partial p_s/\partial E_F)$. In a sheet, one needs to use Fermi-Dirac rather than Boltzmann statistics. Hence, replace L_{Dp}^2 in Eq. (5) with the more general Thomas-Fermi screening length in bulk semiconductor, given by[25] $L_{TFp}^2 = -\epsilon_s/[q^2\partial p/\partial E_F]$, to obtain $L_{Fp} = -2\epsilon_a/[q^2 D\partial p/\partial E_F]$. Substitution of $D\partial p/\partial E_F = \partial p_s/\partial E_F$ yields $L_{Fp} = L_{2D}$. Assuming the first subband alone to be filled, we have $p_s = m_p^*(E_{1p} - E_F)/\pi\hbar^2$ from Eq. (34). Substitution of this p_s in $L_{Fp} = L_{2D} = -2\epsilon_a/[q^2\partial p_s/\partial E_F]$ yields $L_{Fp} = a_B/2$, where $a_B = 4\pi\hbar^2\epsilon_a/q^2 m_p^*$ is the effective Bohr radius.[26]

B. Different permittivities above and below the film

Refer to the derivation of the depletion width on the p-side of the junction, as in Sec. III. When $\epsilon_1 = \epsilon_2 = \epsilon_a$, the plane over which the boundary condition is $E_x = 0$ occurs at $x = 0$. To treat the case of $\epsilon_1 \neq \epsilon_2$, we assume $\epsilon_1 < \epsilon_2$ without any loss of generality. When $\epsilon_1 < \epsilon_2$, the $E_x = 0$ plane occurs at $x = x_0 > 0$. We divide the film into two regions $x > x_0$ and $x < x_0$, and solve for the depletion width in these regions independently, with the boundary condition $E_x = 0$ at $x = x_0$. The resulting depletion width expressions are the same as Eq. (18), except that ETI for $x > x_0$ is $\eta = \epsilon_s(D/2 - x_0)/\epsilon_1 W_{pB}$ and ETI for $x < x_0$ is $\eta = \epsilon_s(D/2 + x_0)/\epsilon_2 W_{pB}$. Since depletion width in the film for $x > x_0$ and $x < x_0$ cannot be different, the ETIs must be equal, i.e., $\epsilon_s(D - 2x_0)/\epsilon_1 W_{pB} = \epsilon_s(D + 2x_0)/\epsilon_2 W_{pB}$, leading to $x_0 = (D/2)(\epsilon_2 - \epsilon_1)/(\epsilon_2 + \epsilon_1)$. Using this expression for x_0, the ETIs reduce to $\epsilon_s D/(\overline{\epsilon_1 + \epsilon_2}/2)W_{pB}$. Thus, the potential distribution in a nanofilm junction with different permittivities above and below the film is the same as that in the case where the two permittivities are replaced by an effective permittivity equal to their average value

$$\epsilon_{eff} = (\epsilon_1 + \epsilon_2)/2\,. \tag{37}$$

The above result, which is derived by considering depletion width, can also be derived from Eq. (26) for φ under linear screening.

C. Interface charge

Refer to Eq. (9). When interface charge $\sigma_f = 0$, the term $\rho + 2\sigma_f/D$ in the numerator of the RHS reduces to ρ. In the presence of σ_f, we let $\rho + 2\sigma_f/D = \rho_{eff}$, where ρ_{eff} is the effective space-charge density, and replace ρ in our derivations by ρ_{eff}. For example, consider the depletion width derivation of Sec. III with $\rho = -qN_A$ on the p-side and $\rho = qN_D$ on the n-side, and $\sigma_f = qN_f$, i.e., $\rho_{eff} = -q(N_A - 2N_f/D)$ on p-side and $\rho_{eff} = q(N_D + 2N_f/D)$ on n-side. Proceeding with this ρ and σ_f, we obtain for W_p the same result as in Eq. (18), except that N_A and N_D in W_{pB}, $V_{bi} = V_t \ln(N_A N_D/n_i^2)$, η and a are replaced by the effective doping levels

$$N_{A,eff} = N_A - 2N_f/D \quad \text{and} \quad N_{D,eff} = N_D + 2N_f/D \tag{38}$$

(the factor 2 in $2N_f/D$ is because of two interfaces—one above and one below). Thus, interface charge can be accounted for by changing the doping by an amount obtained by distributing the interface charge over the film thickness uniformly. Note that, a positive σ_f causes surface depletion in the p-side of the film, reducing the effective D, which is seen in the above model as a reduction in effective doping on p-side. When $N_f = N_A D/2$, from Eq. (38), $N_{A,eff} = 0$ resulting in an infinite depletion width on p-side. This singularity arises because the interface charge itself depletes the entire film on the p-side.

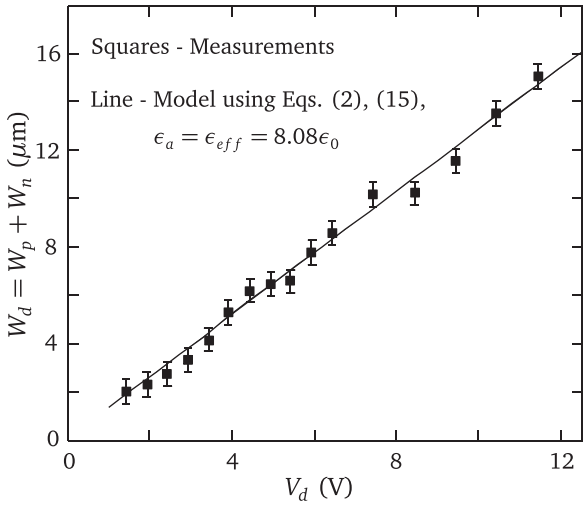

FIG. 6. Comparison between the measured[27] and modelled depletion width versus potential drop behaviors in a reverse biased lateral *p-n* junction realized in a 10 nm InGaAs nanofilm stacked between the ambients of 650 nm GaAs buffer and 175 nm AlGaAs/GaAs-AlAs/AlGaAs multilayer.

VII. COMPARISON WITH MEASUREMENTS AND PRIOR WORKS

In addition to the validation of our model using TCAD simulations presented in Secs. III C and IV B, and numerical calculations presented in Sec. VI A, we compare our work with measurements and theory published in prior works.

In Fig. 6, we compare results of our depletion width model with those obtained from Optical Beam Induced Current (OBIC) measurements.[27] The measurements correspond to a lateral *p-n* junction realized in a 10 nm thick $In_{0.1}Ga_{0.9}As$ film deposited over a 650 nm thick GaAs buffer. The InGaAs film is capped by 175 nm thick composite layer consisting of $Al_{0.33}Ga_{0.67}As$ followed by carbon doped GaAs-AlAs superlattice and $Al_{0.33}Ga_{0.67}As$ layers. The reported hole and electron surface concentrations are $p_s = 4 \times 10^{11}\,cm^{-2}$ and $n_s = 5 \times 10^{10}\,cm^{-2}$. The ETI of the film on the lightly doped *n*-side can be estimated taking n_s/D and p_s/D as the volume doping levels for bulk depletion width calculation. This ETI turns out to be < 0.1, so we use Eq. (15) derived for sheet-like films and Eq. (2) to calculate $W_d = W_p + W_n$. We see good agreement between modelled and measured values assuming $\epsilon_a = \epsilon_{eff} = 8.08\epsilon_0$. This ϵ_{eff} is slightly higher than $7.05\epsilon_0$, which is the average of the ambient permittivities of air above ($\epsilon_1 = \epsilon_0$) and GaAs below ($\epsilon_2 = 13.1\epsilon_0$). This slight increase of ϵ_{eff} can be attributed to the presence of the high permittivity composite cap layer. The linear dependence of W_d on V_d, as in Fig. 6, has also been observed in the capacitance measurements[8] of a lateral *p-n* junction.

It is of interest to distinguish our analysis from prior works. Ref. 28 analyses a lateral *p-n* junction in a sheet and gives $W_p = \epsilon_a V_d/qN_S$, which is 21% smaller than our more accurate formula Eq. (15). Ref. 29 analyses a Schottky contact between a 2DEG and a bulk metal, and Ref. 30 analyses a junction between a 2DEG and a bulk p^+ semiconductor (which is similar to the bulk metal in Ref. 29). These give the depletion width in the 2DEG as $W_{2DEG} = 2\epsilon_a V_d/qN_S$, which is 21% smaller than our more accurate formula $W_{2DEG} = 8\epsilon_a V_d/\pi qN_S$ obtained from Eq. (15) by replacing V_d by $2V_d$ (because a symmetric lateral *p-n* junction in nanofilm can be viewed as an image-charge construction of a Schottky bulk metal-nanofilm junction). So far, no analysis has given a formula for the space-charge tail width W_{pt}. Moreover, Ref. 30 anticipates the space-charge tail to be several Bohr radii (a_B) long, whereas our analysis establishes the tail to be much longer, on the order of $100a_B$.

Refs. 28–30 assume the film to be a sheet. Hence, they do not incorporate the film's thickness, permittivity, volume doping, and interface charge, whose effects are important in many practical nanofilms.[8,31] The prior analysis of a single nanofilm-bulk metal junction[32] considers the effect of non-zero film thickness on the potential distribution under linear screening but not under nonlinear screening from which we derive the depletion width indispensible in practical situations. None of these analyses deals with the realistic situation of different dielectric constants above and below the film. Moreover, they have not been validated against accurate numerical simulations. Our analysis takes all these aspects into account and yields a simple analytical model for the space-charge region that agrees well with numerical simulations and experiments.

VIII. CONCLUSION

We presented an analytical theory of the electrostatics of the space-charge region of lateral p-n junctions in nanofilms, considering the surrounding field. This 2D theory is analogous to the textbook theory of the 1D electrostatics of bulk junctions. It shows that, over the film thickness, the axial field and potential are approximately uniform and the normal field varies linearly. These approximations allow a simultaneous analytical solution of the Poisson's equation in the film and Laplace's equation in the ambient, and lead to simple expressions for the depletion width, the extent of space-charge tails beyond this width and the screening length. The expressions reflect the film's thickness, permittivity, volume doping, interface charge, and possibly different ambient permittivities on its either side, and match with numerical simulations and measurements. In a nanofilm junction, the depletion width is several times that in a bulk junction, and the space-charge tails are even longer. We introduced the concept of ETI to classify nanofilms into sheets, bulk and intermediate sized. The formulas for sheet-like films are as simple as those for the bulk case. The space-charge tail in these films is ten times the depletion width, or a few hundred times the screening length, which is longer than the Debye length in the bulk. The formulas derived should prove useful for the design of nanofilm devices containing lateral *p-n* or even Schottky junctions.

[1]M. Shur, *Physics of Semiconductor Devices* (Prentice-Hall, Inc., 1990).
[2]S. M. Sze and K. K. Ng, *Physics of Semiconductor Devices* (John Wiley & Sons, 2006).
[3]S. Karmalkar, IEEE Trans. Electron Devices **45**, 2187 (1998).
[4]K. Maheswaran and S. Karmalkar, Physica E **44**, 700 (2011).
[5]S. Merchant, E. Arnold, H. Baumgart, S. Mukherjee, H. Pein, and R. Pinker, in *3rd International Symposium on Power Semiconductor Devices and ICs (ISPSD'91)* (IEEE, 1991), pp. 31–35.

[6]M. Bawedin, C. Renaux, and D. Flandre, Solid-State Electron. **48**, 2263 (2004).
[7]Y.-K. Leung, A. K. Paul, J. D. Plummer, and S. S. Wong, IEEE Trans. Electron Devices **45**, 2251 (1998).
[8]C. Wiemann, M. Versen, and A. Wieck, J. Vac. Sci. Technol. B **16**, 2567 (1998).
[9]W. C. B. Peatman, T. W. Crowe, and M. Shur, IEEE Electron Device Lett. **13**, 11 (1992).
[10]M. Shur, W. Peatman, H. Park, W. Grimm, and M. Hurt, Solid-State Electron. **38**, 1727 (1995).
[11]M. Horstmann, K. Schimpf, M. Marso, A. Fox, and P. Kordos, IEEE Electron. Lett. **32**, 763 (1996).
[12]M. S. Choi, D. Qu, D. Lee, X. Liu, K. Watanabe, T. Taniguchi, and W. J. Yoo, ACS Nano **8**, 9332 (2014).
[13]C.-H. Lee, G.-H. Lee, A. M. van der Zande *et al.*, Nat. Nanotechnol. **9**, 676 (2014).
[14]M. Bernardi, M. Palummo, and J. C. Grossman, Nano Lett. **13**, 3664 (2013).
[15]R. Sundaram, M. Engel, A. Lombardo, R. Krupke, A. Ferrari, P. Avouris, and M. Steiner, Nano Lett. **13**, 1416 (2013).
[16]B. Radisavljevic, A. Radenovic, J. Brivio, V. Giacometti, and A. Kis, Nat. Nanotechnol. **6**, 147 (2011).
[17]D. Jariwala, V. K. Sangwan, L. J. Lauhon, T. J. Marks, and M. C. Hersam, ACS Nano **8**, 1102 (2014).
[18]L. Wang, I. Meric, P. Huang *et al.*, Science **342**, 614 (2013).
[19]W. Liu, J. Kang, W. Cao, D. Sarkar, Y. Khatami, D. Jena, and K. Banerjee, IEEE Int. Electron Devices Meet. **2013**, 19.4.1.
[20]R. S. Irving, *Integers, Polynomials, and Rings: A Course in Algebra* (Springer Science & Business Media, 2003).
[21]*Sentaurus Device User Guide* (Synopsys, 2013).
[22]A. De Mari, Solid-State Electron. **11**, 33 (1968).
[23]N. W. Ashcroft and N. D. Mermin, *Solid State Physics* (Brooks Cole, 1976).
[24]J. H. Davies, *The Physics of Low-Dimensional Semiconductors: An Introduction* (Cambridge University Press, 1997).
[25]H. Haug and S. W. Koch, *Quantum Theory of the Optical and Electronic Properties of Semiconductors* (World Scientific, 2004).
[26]T. Ando, A. B. Fowler, and F. Stern, Rev. Mod. Phys. **54**, 437 (1982).
[27]D. Reuter, C. Werner, A. Wieck, and S. Petrosyan, Appl. Phys. Lett. **86**, 162110 (2005).
[28]A. S. Achoyan, A. Yesayan, E. Kazaryan, and S. Petrosyan, Semiconductors **36**, 903 (2002).
[29]S. Petrosyan and A. Y. Shik, Sov. Phys. JETP **69**, 1261 (1989) [Zh. Eksp. Teor. Fiz. **96**, 2229–2239 (1989)].
[30]B. Gelmont, M. Shur, and C. Moglesture, IEEE Trans. Electron Devices **39**, 1216 (1992).
[31]D. Reuter, C. Meier, C. Riedesel, and A. D. Wieck, Semicond. Sci. Technol. **17**, 585 (2002).
[32]A. Achoyan, S. Petrosyan, W. Craig, H. Ruda, and A. Shik, J. Appl. Phys. **101**, 104308 (2007).